



Predicting the onset of condensate droplet departure from a vertical surface due to air flow—Applications to topographically-modified, micro-grooved surfaces

A.D. Sommers^{a,*}, J. Ying^{b,1}, K.F. Eid^{b,1}

^a Department of Mechanical and Manufacturing Engineering, Miami University, 56 Engineering Building, Oxford, OH 45056, USA

^b Department of Physics, Miami University, 35 Culler Hall, Oxford, OH 45056, USA

ARTICLE INFO

Article history:

Received 14 June 2011

Received in revised form 13 January 2012

Accepted 17 January 2012

Available online 11 February 2012

Keywords:

Anisotropic wettability

Contact angle

Air velocity

Drag

Micro-channels

Water droplet

Condensate carryover

ABSTRACT

Air-flow induced water droplet movement on micro-patterned aluminum surfaces consisting of parallel grooves tens of microns in width and depth is considered, and a simple model for calculating the critical air flow force for water droplet departure from vertical surfaces is presented. This model which considers the combined effect of the gravitational, surface tension, and air flow forces on the droplet was found to provide reasonably accurate agreement with experimental data for water droplets 1–25 μL in size. In this method, the user must specify the advancing and receding contact angles of the surface, droplet volume, and micro-channel width and depth (if applicable). When applied to surfaces of varying wettability, the model was shown to calculate the actual critical air velocity to within 15.2% for 89% of the droplet volumes analyzed. For surfaces with parallel micro-channels aligned vertically with gravity and no surface coating, the critical air velocity for water droplet departure was found to be more than 180% higher than the baseline surface (i.e. no micro-channels or coating)—a behavior that was also observed experimentally. Moreover, for micro-grooved samples with a PDMS coating, the required air velocity for movement across the channels was 1.0–1.2 m/s larger than the air velocity required for movement along the channels and only slightly lower than the baseline case. These results suggest that topographically-modified, anisotropic surfaces may be useful in air cooling applications where both heat and mass transfer occur and where the surface micro-channels are aligned parallel to gravity to not only assist in condensate drainage but to also resist the carryover of condensate into the occupied space.

© 2012 Elsevier Inc. All rights reserved.

1. Introduction

The effective removal of water droplets from heat transfer surfaces is important to the overall performance of air-conditioning and refrigeration systems. In air-cooling applications, condensate retention on the heat transfer surface is problematic because it can reduce the air-side heat transfer by occupying heat transfer surface area and increasing the core pressure drop. In addition, the retained condensate provides a site for biological activity which may cause odors and can adversely affect human comfort if it is blown off the heat exchanger and carried downstream into the occupied space creating an unwanted fog. Once a condensate droplet forms on the fin surface, it continues to grow and coalesce with other droplets until gravitational, capillary, or air flow forces remove it. Therefore, it is important to understand how condensate is retained on the heat-transfer surface and how these forces affect the critical air flow force required for condensate blow-off and removal. While the effects of condensate retention on air-side heat transfer are

generally well-known, there are relatively few papers which attempt to predict the onset of droplet departure from a vertical surface under the combined effects of gravitational and air flow forces. Moreover, while several papers describe the role and interaction of forces on retained droplets, the authors are not aware of any paper that seeks to specifically address this interaction on topographically-modified, micro-grooved surfaces—the focus of this work. Thus, understanding the shape and size of a water droplet adhered to a surface and accurately calculating the magnitude of the air flow force are the keys to predicting the onset of condensate droplet departure from a vertical heat transfer surface.

The objective of this work was to devise a method for predicting the critical air velocity for water droplet departure from a vertical surface using only a few simple parameters that can be easily measured—advancing and receding contact angles, droplet volume, and in the case of micro-grooved surfaces, the width and depth of the micro-channels. Thus, the engineering value of this research rests in its direct application to the modeling and control of condensate on heat transfer surfaces used in dehumidification and air-cooling systems. This work also provided a better understanding of the anisotropic wettability of a highly controlled surface microstructure which might facilitate new surface designs with improved

* Corresponding author. Tel.: +1 513 529 0718; fax: +1 513 529 0717.

E-mail address: sommerad@muohio.edu (A.D. Sommers).

¹ Tel.: +1 513 529 1933; fax: +1 513 529 5629.

Nomenclature

A	cross-sectional area (mm ²)	ϕ	azimuthal angle (°)
C_D	drag coefficient	γ	surface tension (N m ⁻¹)
D	droplet major diameter (mm)	η	droplet migration angle (°)
g	acceleration due to gravity (m s ⁻²)	φ	surface area fraction used in the Cassie model—ratio of wetted surface area to projected area (Eq. (24))
h	droplet height (mm)	μ	air viscosity (kg m ⁻¹ s ⁻¹)
L	half of a droplet's major axis (mm)	θ	apparent contact angle (°)
m	droplet mass (mg)	ρ	air density (kg m ⁻³)
r	surface roughness factor (Eq. (23))	ψ	surface parameter (Eq. (20))
Re_D	Reynolds number, $\rho UD/\mu$	ζ	droplet base contour radius (mm)
U	air velocity (m s ⁻¹)		
V	droplet volume (μ L)		
w	half of a droplet's minor axis; etched pillar width (mm, μ m)		
x, y, z	coordinate directions		
		Subscripts	
		adv	advancing
		crit	critical
		eq	equivalent
		min	minimum
		max	maximum
		rec	receding
Greek Symbols			
α	surface inclination angle (°)		
β	droplet aspect ratio, L/w		
δ	channel etch depth (μ m)		

liquid drainage behavior. Thus, as part of this modeling effort, the influence of the underlying microstructure on the critical air velocity for droplet departure was explored. Because droplet shapes on surfaces with anisotropic wetting behavior are different from those on conventional, isotropic surfaces, it was found that surfaces manufactured with parallel micro-channels (with or without surface coating) significantly affected the critical air velocity.

2. Literature review

In an early study of droplets on grooved substrates, Oliver, Huh, and Mason examined droplets of PPE and mercury on parallel-grooved nitrocellulose surfaces and found that the mercury droplets were nearly spherical while the PPE droplets were cylindrical [1]. Using a mechanistic approach, Oliver and co-workers showed that the Cassie–Baxter equation was not valid for the case of cylindrical droplets on these parallel-grooved surfaces and developed a new expression for the apparent contact angle from a two-dimensional force balance. This new expression, however, did not consider air flow.

Morita et al. offered insight into the anisotropic wetting of micro-patterned fluoroalkylsilane monolayer surfaces with alternating hydrophilic/hydrophobic lines of width 1–20 μ m [2]. They observed that the static and dynamic contact angles of a droplet oriented orthogonally to the stripes were 10–30° larger than those of the droplet oriented parallel to the stripes. Sliding angle data showed low tilt angles for droplets sliding parallel to the stripes, but droplets sliding orthogonally to the stripes resisted tilt angles of more than 80°. Yoshimitsu et al. studied the sliding behavior and contact angle variation of water droplets on hydrophobic pillar and groove structures prepared from a silicon wafer by dicing it and then coating it with fluoroalkylsilane [3]. They found that the dependence of the sliding angle on the weight of the water droplet was smallest for the parallel direction in the groove structure, followed by the pillar structure, and finally by the orthogonal direction in the groove structure. The only paper identified that addresses the condensation of water vapor onto a superhydrophobic grooved surface is the work of Narhe and Beysens [4]. In this work, silicon substrates were prepared using the same technique outlined by Yoshimitsu et al. and treated by silanization. The contact angles were $130^\circ \pm 2^\circ$ and $110^\circ \pm 2^\circ$ in the directions orthogonal and parallel to the groove, respectively.

In another related work, Chen et al. examined the apparent contact angle and shape of water droplets on parallel-grooved surfaces using both numerical and experimental approaches [5]. Equilibrium drop shapes were predicted numerically by minimizing the system free energy while simultaneously constraining the droplet volume to a fixed value. In their model, the initial droplet shape and the number of occupied channels were specified as inputs. It was found that multiple equilibrium shapes were possible, and droplets were observed to be pinned against the pillars, both numerically and experimentally.

Extrand and Kumagai studied contact angle hysteresis, droplet shape, and the retentive force for water and ethylene glycol droplets at the critical condition on polymer and silicon surfaces using a tiltable plane [6]. They found that surfaces with large contact angle hysteresis produce more elongated drops. More recently, Tadmor et al. measured lateral adhesion forces associated with a solid–liquid interface and found that the lateral retention force is a growing function of the droplet resting time [7,8]. In a numerical study of droplets at the critical condition, Dimitrakopoulos and Higdon solved for the droplet configuration that produced minimum contact angle hysteresis (i.e. $\theta_A - \theta_R$) for a specified advancing angle θ_A and Bond number [9].

Dussan and Chow also studied static droplet shapes at critical conditions on an inclined surface for a droplet contact line with straight-line segments on the sides [10]. In this view, the droplet was assumed to be elongated and parallel-sided. This analysis, however, was valid only in the limit of small contact angles, and Dussan later extended this work to allow for larger contact angles [11]. The model provided closed-form expressions for the maximum volume, speed, and wetted area of a droplet on a surface of inclination, α , but it required knowledge of the advancing and receding contact angles, θ_A and θ_R , as well as the slope of the contact angle with respect to the speed of the contact line, R and A . The most limiting restriction of this analysis was its assumption of small contact angle hysteresis. Dussan later included the effects imposed by the motion of the surrounding fluid, but again the analysis was limited to a droplet with small contact angles and small hysteresis [12]. Other relevant works include Merte and Son and Merte and Yamali who studied the equilibrium shape and departure size of two-dimensional dropwise condensation on a vertical surface [13,14]. A model was developed which minimized the total energy of the droplet using techniques from variational calculus. Simulation

results were compared against experimental data with reasonable agreement found. In this two-dimensional model, however, the air flow force was not considered.

In two recent reports by El Sherbini and Jacobi, droplet shapes were studied experimentally [15,16]. The droplet shape was approximated using a ‘two-circle method’ in which the droplet profile is fitted with two circles sharing a common tangent at the apex of the droplet. The volume was then calculated by integrating the profile around the circumference of the base. This method which was developed for conventional surfaces of homogeneous roughness was found to accurately predict the volume of droplets, knowing only the contact angle and shape of the three-phase contact line. In this study, the two-circle approach was adopted and modified to more accurately calculate the frontal area of the droplet.

Korte and Jacobi examined the effect of condensate retention on the thermal performance of plain fin, round-tube heat exchangers having fin spacing much larger than the height of retained droplets [17]. A model was also developed from a three component force balance (i.e. gravity, surface tension, and drag force) for predicting the mass of retained condensate and compared to steady-state retention data. The model was found to be reasonably successful in predicting retained condensate under relatively restricted operating conditions; however, the heat exchangers studied in this work were oriented in a down-flow configuration and the critical air flow force was not explored.

Several papers were found involving the calculation of the drag force on single particles such as bubbles, droplets, and rigid spheres [18–38]. For example, Al-Hayes and Winterton [18] performed an extensive series of measurements for bubbles detaching from a surface into a flowing liquid and then used these data to propose new expressions for the drag forces experienced by a bubble on a submerged surface. The liquids that were tested included water, water with a surfactant and ethylene glycol. The droplet contact angles varied from 22° to 90° (similar to present work), and they found $C_D = 1.22$ for $20 < Re_D < 400$. However, in this work, the Reynolds number is greater than 900 making the extrapolation of these data especially tenuous. In a paper on bubble detachment from a vertical wall, Van Helden et al. [19] also briefly discussed the drag force exerted on a bubble. Since bubble lift-off was in the x -direction, the drag force was not involved; however, Van Helden et al. referenced the paper by Al-Hayes and Winterton [18] noting that the drag coefficient would likely be different than $C_D = 1.22$ due to flow separation around the bubble since the bubble Reynolds number was much higher in their case.

In addition, several papers were also found which considered the transport characteristics of bubbles in two-phase flows including the influence of the drag force and bubble–bubble interactions. In gas–liquid two-phase flows, the drag coefficient is especially difficult to determine since gas bubbles can be deformed due to liquid turbulence, interface interaction and phase change. In Ishii and Chawla [27], constitutive relations for the drag coefficient of bubbles in various flow regimes were proposed. A comparison of their theoretical predictions with over 1000 experimental data showed satisfactory agreement; however, these relations were derived assuming similarity between drag coefficients in single and multiple particle systems and thus were intended for use in two-phase flows.

Others have studied the deformation and breakup of liquid droplets in turbulent gas flows. Unfortunately, there is no consensus about the variation of the drag coefficient for a deforming liquid droplet in these types of flows. Prandtl [28] assumed that the drag coefficient C_D had a value close to 0.5 and that its subsequent deformation in the flow was accompanied by an increase in that value. Volynskii [29] and Lane [30] both assumed a constant value of 0.44 corresponding to the self-similar regime for flow over

a sphere (i.e. $Re_D = 1000–300,000$). Volgin and Yugai [31] also studied liquid droplets in gas flows and observed a tendency for the drag coefficient to fall within a narrow range of Reynolds numbers from 2000 to 2600 for droplets 2.0–3.0 mm in diameter. Unfortunately, the minimum value of the drag coefficient could not be established, and Volgin and Yugai attributed this decrease to liquid circulation within the droplet which tended to mitigate the importance of the pressure drag. Other germane studies involving the calculation of the drag force on single particles include those by Uhlherr and Sinclair [32] and Warnica et al. [33] as well as Morsi and Alexander [34], Beard and Pruppacher [35], Mei and Klausner [36], Klausner et al. [37], and Zeng et al. [38]. In these later works, vapor bubble detachment in forced convection boiling is discussed, and a mechanistic model (which includes the drag force) is developed. It is important to note, however, that the drag force was only considered at the point of bubble departure (i.e. bubble was raised up on the surface).

In summary, very few papers were found in the literature which attempt to model the combined effect of gravitational, surface tension, and air flow forces on liquid droplets, and only a few studies were found involving the behavior of liquid droplets on parallel, micro-grooved surfaces where droplets have been reported to exhibit an elongated, parallel-sided base contour shape. Although significant research has already been reported on analytical and numerical methods for calculating droplet forces, no method was found that specifically addressed the calculation of the drag coefficient for condensate droplets on a heat transfer surface and/or the critical air flow force required for droplet blow-off in air-cooling applications. Therefore, new models and calculation methods are needed if functional topography is to be used for the purpose of controlling condensation and water drainage on heat transfer surfaces.

3. Background and experimental methodology

The objective of this research was to better understand how the anisotropy of a micro-grooved surface would affect water droplet shedding due to air flow and to develop a model for predicting the onset of the condensate carryover phenomenon. To that end, water droplet contact angles were measured using a Ramé-Hart goniometer, and still images of water droplets on vertical surfaces were obtained in an open-loop wind tunnel using a charge coupled device (CCD) camera. In the following sections, a more detailed description of the surface fabrication procedure and experimental setup is presented.

3.1. Surface preparation

Parallel channels approximately tens of microns in width and depth, running the length of the surface, were etched into plates of aluminum alloy 1100 (99.9% pure Al), 63.5 mm by 63.5 mm by 3.2 mm in size. Aluminum was chosen because it is naturally hydrophilic and is the material of choice in many heat and mass transfer applications. The fronts of the plates were machine buffed to ensure good surface reflectivity, with care taken to ensure that they remained flat. This care is necessary to minimize errors during the transferring of the mask pattern to the photoresist layer during UV exposure. To prepare the plates for photolithography and chemical etching, the plates were cleaned with acetone for up to 15 min in an ultrasonic bath and then dried using a stream of nitrogen gas. Next, a technique developed by Guo et al. was used, and the plates were immersed in 4 wt.% NaOH aqueous solution for two hours to increase the initial surface roughness [39]. In their work, Guo et al. increased the water contact angle from approximately 67° to more than 160° by immersing an aluminum surface

in sodium hydroxide for several hours and then spin coating a layer of poly(dimethylsiloxane) vinyl terminated (PDMSVT) on the surface.

3.2. Photolithographic method

Standard photolithographic practices were then used to impart the anisotropic pattern to the surface and prepare the plates for wet etching. First, a positive photoresist (i.e. S1813) was spin-coated onto the aluminum surface using a Laurell spinner to produce a uniformly thick layer. The thickness of S1813 layer was 1.8 μm when spun at 2000 rpm for 40 s. Because the total energy needed for proper exposure is dependent on the thickness of the film, a thin and homogeneous film is necessary for high resolution. In all cases, the plates were chemically cleaned to remove contamination and heated to drive off any moisture that may be present on the surface prior to spinning. Following this process, a Myriad System 2001 Mask Aligner was used to align a photomask over the aluminum substrate and expose the photoresist to UV light. The photomask used in this project (i.e. soda-lime base with a chrome coating) contained parallel micro-grooves 15 μm , 50 μm , or 100 μm in width. Prior to exposure, the aluminum plate was soft baked to reduce the solvent content in the resist layer and thus prevent mask sticking. After exposure, the plate was developed using a Shipley Microposit Developer CD-26. Table 1 shows the relevant photolithography parameters. The surfaces were then etched using a Transene Aluminum Etchant, Type A (i.e. 80 wt.% phosphoric acid, 5% nitric acid, 5% acetic acid, and 10% distilled water) at 50 $^{\circ}\text{C}$ with an etching rate of approximately 660 nm/min.

3.3. Surface modification

After etching, the photoresist was then stripped in acetone, and the plates were rinsed in deionized water for 3 min and characterized using a surface profilometer. The plates were then analyzed using a Field Emission Scanning Electron Microscope (FE-SEM) as well as a profilometer to determine the surface geometry accurately. Scanning electron microscope images of a couple representative surfaces are included in Fig. 1. The measured depth of the channels after etching for 25 and 30 min were 6.8 μm and 10 μm , respectively. Further surface modification was performed using poly(dimethylsiloxane) vinyl terminated (PDMSVT) as shown in Fig. 2 in combination with a 1 wt.% Sylgard 184 silicone elastomer curing agent obtained from Dow Corning Company. The modified films were obtained by spin-coating at a speed of 3000 rpm for 30 s and then curing on a hot plate at 120 $^{\circ}\text{C}$ for 20 min. By spinning at 3000 rpm, the PDMSVT formed a relatively thick film on the surface (approx. 13 μm). PDMSVT is a low surface energy material which can be used to increase the hydrophobicity of the underlying surface. This hydrophobicity is further amplified by the roughness of the underlying substrate.

3.4. Experimental apparatus and instrumentation

The apparent contact angles and base dimensions of the droplets were obtained using a Ramé-Hart goniometer in combination with a high-resolution CCD camera. Droplets were photographed

Table 1
Standard photolithographic process performed on Al plates.

Photoresist	Spinning	Soft bake	Exposure	Developer	Post bake
S1813	40 s @ 2000 rpm	110 $^{\circ}\text{C}$ 1 min	3 s	CD-16 (40s)	125 $^{\circ}\text{C}$ 2 min

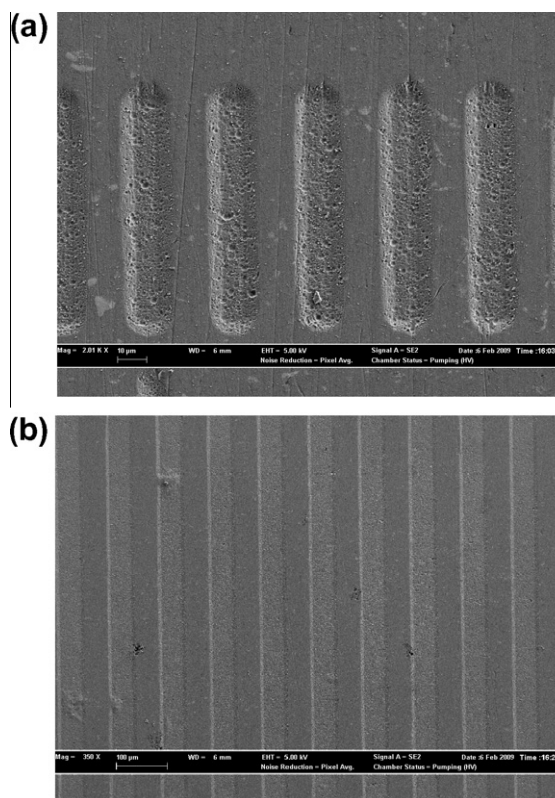


Fig. 1. SEM images of Al surfaces after etching with Transene Aluminum Etchant Type A for 30 min: (a) 15 μm wide parallel channels, (b) 50 μm wide parallel channels.

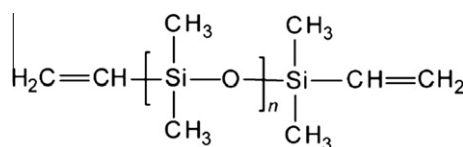


Fig. 2. Chemical structure of poly(dimethylsiloxane) vinyl terminated (PDMSVT).

with the etched channels aligned parallel to gravity as shown in Fig. 3 with images recorded at azimuthal angles of 0 $^{\circ}$ and 90 $^{\circ}$. The grooves were aligned with gravity because that configuration has been shown to be the most promising for promoting drainage. In this view, the advancing contact angle coincides with the location $\varphi = 0^{\circ}$ on the surface, and the receding contact angle coincides with the location $\varphi = 180^{\circ}$ on the surface. Typical uncertainty in the measured contact angle was 1–2 $^{\circ}$ while typical uncertainty in droplet diameter was 2–3% with the maximum uncertainty not exceeding 7%. A list of all manufactured surfaces and their respective contact angles can be found in Table 2.

An open-loop wind tunnel (shown in Fig. 4) was used in these experiments to measure the air-flow force required to overcome the surface tension retaining force and cause water droplet motion (i.e. the incipience of condensate carryover). The air flow was drawn from the inlet plenum, through honeycomb flow straighteners, screens, and a 9.5:1 area contraction into the test section at rates up to approximately 150 m^3/min . The test section (30.48 cm \times 30.48 cm \times 60.96 cm) was constructed from anodized 6061 aluminum and permitted both flow measurements upstream and downstream of the vertical surface and visual access to the specimen. The specified airspeed range for this wind tunnel is 4.5 m/s to 65+ m/s with an associated turbulence level of less than 0.2%.

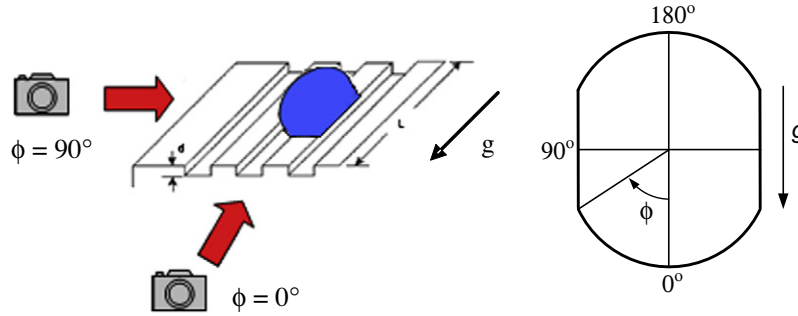


Fig. 3. Contact angle measurement configuration with channels oriented parallel to gravity.

Table 2
List of manufactured surfaces.

	Channel spacing, w_1	Channel width, w_2	Channel depth, δ	Advancing angle, θ_A	Receding angle, θ_R	Hysteresis
Baseline surface	–	–	–	107.1°	75.2°	31.9°
Sample 1 (with PDMS)	40 μm	60 μm	10 μm	116.4°	90.4°	26.0°
Sample 2 (with PDMS)	$\sim 43 \mu\text{m}^a$	$\sim 57 \mu\text{m}^a$	6.8 μm	122.3°	88.0°	34.3°
Sample 3 (no coating)	36 μm	64 μm	12 μm	102.2°	31.7°	70.5°

^a Not measured directly.

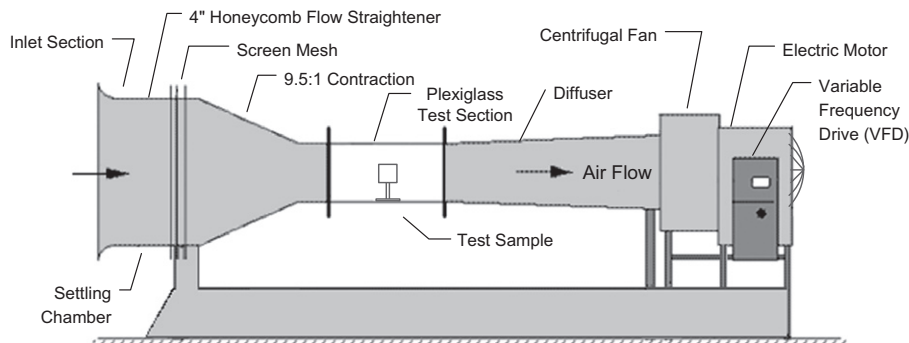


Fig. 4. Open loop wind tunnel used to performed the critical air velocity measurements.

For these experiments, the aluminum test sample was oriented vertically inside the wind tunnel parallel to the direction of the air stream. After a water droplet of known volume was injected onto the sample using a high-precision micro-syringe, then the blower was activated. If droplet motion was not immediately observed, the fan was turned “off.” The fan speed was then incrementally increased using a PID controller, and a new droplet was placed on the sample. When droplet motion was first detected, the air velocity was measured using a hot-bulb anemometer to determine the “critical air flow rate” for droplet motion for a given size on the test surface. For the flow rates examined in these experiments, the local velocity at the droplet half height was taken as equal to the measured mainstream velocity since the boundary layer is thin. (According to the Blasius velocity profile, the local velocity at the droplet half height is within 99.9% of the mainstream velocity for the location on the surface where the droplet was placed.) Because a new droplet was placed on the surface prior to each performed test and uniform flow conditions are achieved soon after the activation of the fan, losses due to evaporation were assumed to be minimal.

To check this assumption, however, small water droplets were placed on a digital balance with a readability of $\pm 0.0001 \text{ g}$ and weighed continuously for a period of 20 min. For 10 μL and 60 μL sessile droplets, the evaporation rate was found to be 0.00026 g/min and 0.00054 g/min, respectively. Thus, the evaporative losses

after three minutes would be 7.8% and 2.7%, respectively. In this study, contact angle measurements were typically performed within a couple of minutes of the droplet being placed on the surface. Moreover, contact angle measurements have been shown to vary very little with the droplet volume as suggested by a recent study [40]. For the critical velocity measurements, a new droplet was injected on the surface before each test thus minimizing the effect of evaporation. Thus, for the range of droplet volumes examined (i.e. 5–70 μL), the effect of evaporation was deemed small.

4. Calculating the critical air velocity for water droplet departure

For the case of an idealized water droplet on a vertical surface, the calculation of the critical air flow force required for water droplet departure can be found using a three-component force balance on the droplet as shown below in Fig. 5 such that:

$$F_{g,x} + F_{s,x} + F_{d,x} = 0 \quad (1)$$

where $F_{g,x}$ represents the gravitational force, $F_{s,x}$ represents the surface tension force, and $F_{d,x}$ represents the air flow force in the x -direction.

The x -component of the gravitational force is simply calculated as

$$F_{g,x} = \rho \cdot V \cdot g \cdot \sin \alpha \cdot \cos \eta \quad (2)$$

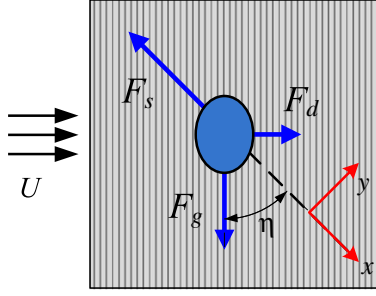


Fig. 5. Schematic showing relevant forces on a condensate droplet.

where V is the volume of the water droplet, α is the angle of inclination of the surface (i.e. $\alpha = 90^\circ$ for a vertical surface), and η is the angle of droplet migration along the surface (see Fig. 5). The calculation of the surface tension force is found by performing the integration

$$F_{s,x} = -\gamma \int_0^{2\pi} \zeta \cos \theta \cos \phi d\phi \quad (3)$$

where γ is the liquid surface tension, ζ is the local droplet base radius, θ is the local droplet contact angle, and ϕ is the azimuthal angle measured around the base of the droplet. In this view, the contact angle at $\phi = \eta$ is assumed to be the advancing contact angle, θ_{adv} , and the contact angle at $\phi = \pi + \eta$ is assumed to be the receding contact angle, θ_{rec} . Furthermore, the contact angle was assumed to vary monotonically as described by El Sherbini and Jacobi [15] such that

$$\cos \theta(\phi) = 2 \frac{\cos \theta_{max} - \cos \theta_{min}}{\pi^3} \phi^3 - 3 \frac{\cos \theta_{max} - \cos \theta_{min}}{\pi^2} \phi^2 + \cos \theta_{max} \quad (4)$$

For a horizontal droplet, $\theta_{min} = \theta_{max}$; whereas for a droplet at the critical condition, $\theta_{max} = \theta_{adv}$ and $\theta_{min} = \theta_{rec}$. The local droplet base radius which is also a function of the azimuthal angle, ϕ , was modeled using the cubic equation proposed by Chen et al. [5] and adopted by Sommers and Jacobi [41]. Rearranged to be explicit in terms of ζ , this equation can be written as:

$$\zeta(\phi) = \left[\left(\frac{|\cos \phi|}{L} \right)^3 + \left(\frac{|\beta| \sin \phi}{L} \right)^3 \right]^{-1/3} \quad (5)$$

where L is the droplet major radius. In exploring the suitability of various base-contour shapes for droplets, the elliptical shape was found to be inadequate since it did not represent the parallel-sided shape of droplets on micro-grooved surfaces. In this way, Eq. (5) which is 'flatter' than an ellipse provides a slightly more realistic representation of the actual shape of droplets on these surfaces. Because the air flow force affects the water droplet shape (and thus the local droplet contact angles), the following equation was ultimately adopted for the calculation of the surface tension force

$$F_{s,x} = -A\gamma \int_0^{2\pi} \zeta \cos \theta \cos \phi d\phi \quad (6)$$

where A represents a scaling factor. (Note: The empirical relationship developed by El Sherbini and Jacobi [15] was for the case of no air flow.) The scaling factor was determined by checking the goodness of fit of the model with the baseline data. The adopted value (i.e. $A = 1.40$) was also shown to agree well when the baseline surface was tested horizontally in the wind tunnel to eliminate the influence of gravity on the droplet at the onset of droplet motion. By equating the forces on the droplet at the onset of droplet motion (i.e. $F_s = F_d$) and using a theoretical drag coefficient gleaned

from the literature, the scaling factor could be checked. Reasonably good agreement was found across a range of examined droplet volumes (i.e. 5–60 μL). These tests are described in more detail in the following section.

The calculation of the drag force was performed using the equation

$$F_{d,x} = \frac{1}{2} \cdot C_D \cdot \rho_{air} \cdot U^2 \cdot A_{proj} \cdot \sin \eta \quad (7)$$

where C_D is the drag coefficient, ρ_{air} is the density of the air, U is the mainstream air velocity, A_{proj} is the projected area of the droplet, and η is the angle of droplet migration along the surface. The drag coefficient was determined experimentally and then checked against values found in the technical literature as will be discussed in the following section. The projected area of the droplet was calculated using two circles (i.e. C1 and C2) to fit the profile of the droplet as shown in Fig. 6 following the methodology outlined by El Sherbini and Jacobi [16]. Using this method, Eq. (8) was then derived to calculate the projected area such that:

$$A_{proj} = \iint_A x dx dy \quad (8a)$$

$$A_{proj} = \pi \frac{L_1^2}{(\sin \theta_1)^2} \frac{\theta_1}{2\pi} - \frac{1}{2} \frac{L_1^2}{\tan \theta_1} + \pi \frac{L_2^2}{(\sin \theta_2)^2} \frac{\theta_2}{2\pi} - \frac{1}{2} \frac{L_2^2}{\tan \theta_2} \quad (8b)$$

for $\theta_1 < 90^\circ$, $\theta_2 < 90^\circ$

$$A_{proj} = \pi \frac{L_1^2}{(\sin \beta_1)^2} \frac{\theta_1}{2\pi} + \frac{1}{2} \frac{L_1^2}{\tan \beta_1} + \pi \frac{L_2^2}{(\sin \theta_2)^2} \frac{\theta_2}{2\pi} - \frac{1}{2} \frac{L_2^2}{\tan \theta_2} \quad (8c)$$

for $\theta_1 > 90^\circ$, $\theta_2 < 90^\circ$

where

$$L_1 = \frac{DL_f}{1 + L_f} \quad (9)$$

$$L_2 = \frac{D}{1 + L_f} \quad (10)$$

$$L_f = \frac{\sin \theta_1 (1 - \cos \theta_2)}{\sin \theta_2 (1 - \cos \theta_1)} \quad (11)$$

where D represents the major diameter of the droplet (i.e. 2ζ) as shown in Fig. 6, θ_1 is the advancing contact angle, θ_2 is the receding

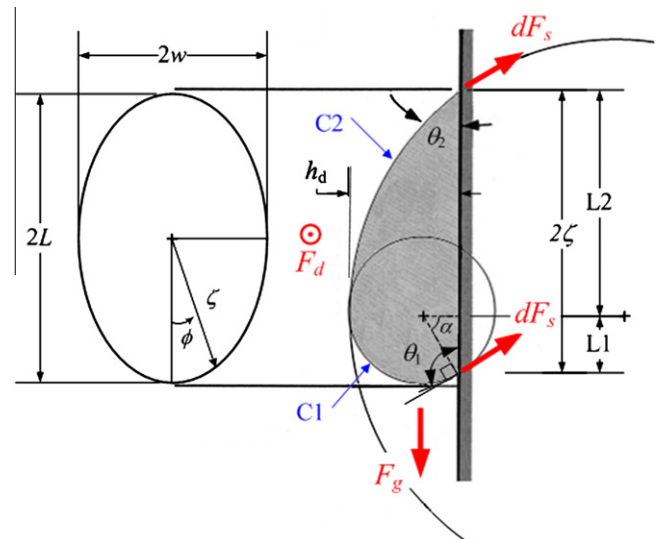


Fig. 6. Schematic showing the two circles used to calculate the projected area of the droplet.

contact angle, and $\beta_1 = (\pi - \theta_1)$. For the baseline surface, it was shown that this “two-circle method” predicts 4% more projected area than the one-circle method; whereas for the micro-grooved surfaces examined in this study, the “two-circle method” predicted about 3% less projected area than the one-circle method.

The angle of droplet migration was determined using calculated values for F_s and F_g which are known *a priori* for a specified droplet volume and surface wettability (i.e. θ_1 and θ_2) such that

$$\eta = \arccos\left(\frac{F_g}{F_s}\right) \quad (12)$$

where

$$F_g = \rho Vg \quad (13)$$

$$F_s = -A\gamma \int_0^{2\pi} \zeta \cos \theta \cos \phi d\phi \quad (14)$$

as depicted in Fig. 5.

5. Determination of the drag coefficient

The drag coefficient was determined by measuring the critical velocity necessary for the onset of droplet motion in the wind tunnel when the baseline surface was oriented horizontally to eliminate the influence of gravity on the droplet. Because the droplet is less elongated and droplet migration occurs along a straight line, the surface tension force is also more readily calculated on the horizontal surface than on the vertical surface where droplet deformation complicates the calculation of the surface tension force. By equating the forces on the droplet at the onset of droplet motion (i.e. $|F_s| = |F_d|$), the drag coefficient could be inferred such that:

$$C_D = \frac{|2A\gamma \int_0^{2\pi} \zeta \cos \theta \cos \phi d\phi|}{\rho_{\text{air}} U^2 A_{\text{proj}}} \quad (15)$$

In addition, the technical literature was consulted for applicable values (see Table 3). One of the most commonly cited studies was Al-Hayes and Winterton [18] who examined bubbles detaching from a solid surface in flowing liquids. The equilibrium contact angle ranged from 22° to 90°, and the drag coefficient was found to be:

$$C_D = 1.22 \quad \text{for } 20 < Re_D < 400 \quad (16)$$

$$C_D = 24/Re_D \quad \text{for } 4 < Re_D < 20 \quad (17)$$

where Re_D was defined using the local boundary-layer velocity at the droplet half-height and a location midway across the surface. In the present work, the calculated Reynolds number, Re_D , ranged from 1500 to 2500 excluding the use of these published experimental values. (Note: In this study, the mainstream velocity was used in defining the Reynolds number since the boundary layer is thin and according to the Blasius velocity profile, the local velocity at the droplet half-height is within 99.9% of the mainstream velocity.)

Of the papers found containing values or correlations for rigid spheres or bubbles, the value of the drag coefficient varied from 0.35 to 0.45 for $1500 < Re_D < 2500$ as shown in Table 4. (Note: No paper was found which specifically addressed truncated spheres or bubbles detaching from solid surfaces within this Re_D regime.) Both the experimentally determined values found using Eq. (15) (see Table 5) and those gleaned from the literature are plotted in Fig. 7. In this figure, the correlation developed by Beard and Pruppacher [35] for rigid spheres for $200 < Re_D < 4000$ is shown where

$$C_D = 0.28 + \frac{6}{\sqrt{Re_D}} + \frac{21}{Re_D} \quad (18)$$

Reasonable agreement between the various methods was observed. For the present study where $1500 < Re_D < 2500$, a constant value (i.e. $C_D = 0.44$) was used for all cases since the flow regime

was not expected to change over this Re_D range and the uncertainty in C_D was already fairly high. This value corresponds to the self-similar regime for flow over a sphere [29,30]. Should new experiments or computations provide updated drag coefficients for droplets on surfaces, that information could be easily adopted into the existing model. With the drag coefficient now prescribed, Eq. (1) can be rearranged and solved explicitly for the critical air velocity such that:

$$U_{\text{crit}}^2 = \frac{2\left(-A\gamma \int_0^{2\pi} \zeta \cos \theta \cos \phi d\phi - \rho Vg \sin \alpha \cos \eta\right)}{\rho_{\text{air}} C_D A_{\text{proj}} \sin \eta} \quad (19)$$

6. Treatment of the anisotropic surface roughness

The overall objective of this work was to create a general model that could be applied to anisotropic fin surface designs. Through the specification of only the advancing and receding contact angles, droplet volume, and micro-channel geometry (if applicable) as input parameters, it was hoped that a general model could be created which would enable the user to predict droplet departure for various modified surfaces having an underlying surface roughness and/or chemical coating when experiencing an airflow force. For a homogeneous surface, the surface retentive force is usually calculated by integrating the local surface tension force along the droplet contact line (see Eq. (6)). However, for a surface with channels, the contact line may be broken and vary in length at different locations on the surface (i.e. Cassie–Baxter mode of wetting). Alternatively, the length of the contact line may be increased due to additional contact within the channels (i.e. Wenzel mode of wetting). This can add considerable complexity and uncertainty to force-based models since accurate modeling of the contact line is imperative for accurate calculation of the surface tension force. For this reason, a single parameter which closely models the effect of the surface roughness on the contact line would be highly desired.

In the case of parallel micro-channels, one possibility is to use the geometry of the underlying surface micro-structure to scale the length of the contact line. For example, for a micro-structured surface exhibiting Wenzel's mode of wetting (see Fig. 8) with channels of width w_1 and depth δ , the ratio of the contact line length on this surface to the original contact line length on the baseline surface would be:

$$\psi = \frac{w_1 + 2\delta + w_2}{w_1 + w_2} \quad (20)$$

In the case where $w_1 = w_2$, this expression simplifies to:

$$\psi = \frac{w + \delta}{w} \quad (21)$$

where $w = w_1 = w_2$. In this approach, the surface tension force is calculated using the following expression:

$$F_{s,x} = -A\gamma\psi \int_0^{2\pi} \zeta \cos \theta \cos \phi d\phi \quad (22)$$

where $\cos \theta$ is defined as before using Eq. (4). For the surfaces studied experimentally in this work, $\psi = 1.0$ (Baseline), $\psi = 1.2$ (sample 1), $\psi = 1.136$ (sample 2), and $\psi = 1.24$ (sample 3).

7. Results and discussion

Testing in the wind tunnel was performed on the baseline surface, sample 1 (hydrophobic surface) sample 2 (hydrophobic surface), and sample 3 (hydrophilic surface). As discussed earlier,

Table 3
Published drag coefficient studies.

n	C_D relationship	Type	Range	Reference
1	$C_D = 24/Re_D$ for $4 < Re_D < 20$ $C_D = 1.22$ for $20 < Re_D < 400$	Bubbles in flowing liquids	$4 < Re_D < 400$	[18]
2	$C_D = 0.44$ (assumed constant)	Deformable liquid droplets in gas flow	$2.0 < D < 5.0$ mm turbulent flow	[29,30]
3	$C_D \approx 0.45$	Rigid spheres	$Re_D = 1000$	[34]
4	$\log C_D = 1.6435 - 1.1242w + 0.1558w^2$ where $w = \log(Re_D)$	Spheres	$260 < Re_D < 1500$	[21]
5	$C_D = 0.28 + \left(\frac{6}{\sqrt{Re_D}}\right) + \left(\frac{21}{Re_D}\right)$	Rigid spheres	$200 < Re_D < 4000$	[35]
6	$C_D = 0.133 \left(1 + \frac{150}{Re_D}\right)^{1.565} + 4 \left(\frac{u'}{U_R}\right)$ where u'/U_R is the relative turbulence intensity	Rigid spheres	$50 \leq Re_D \leq 700, 0.07 \leq u'/U_R \leq 0.5$	[32]
7	$C_D = 24 \left(1 + 0.1Re_D^{0.75}\right) / Re_D$	Bubbles	$100 < Re_D < 10,000$	[27]

Table 4
Drag coefficient values for rigid spheres and bubbles.

Reynolds number, Re_D	Uhlherr and Sinclair [32]	Clift et al. [21]	Beard and Pruppacher [35]	Ishii and Chawla [27]
500	0.56	0.55	0.59	0.56
750	0.51	0.50	0.53	0.49
1000	0.48	0.47	0.49	0.45
1250	0.46	0.45	0.47	0.42
1500	–	0.44	0.45	0.40
1750	–	–	0.44	0.38
2000	–	–	0.42	0.37
2250	–	–	0.42	0.36
2500	–	–	0.41	0.35

Table 5
Experimentally determined drag coefficients.

Droplet volume (μL)	Air velocity (m/s)	Calculated C_D ($A = 1.00$)
10	10.07	0.413
15	9.79	0.389
20	9.08	0.416
30	8.74	0.399
40	8.14	0.423
50	7.83	0.428
60	7.51	0.441

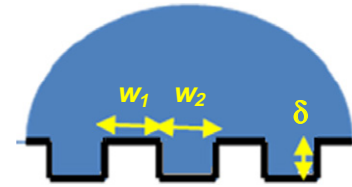


Fig. 8. A substrate of high surface energy satisfying Wenzel's mode of wetting.

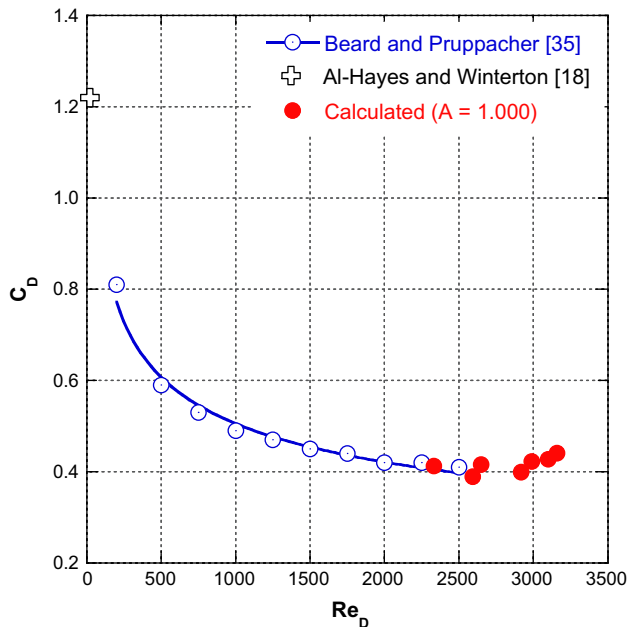


Fig. 7. Plot of theoretical drag coefficient for rigid spheres and experimentally determined values found using Eq. (15).

samples 1–3 were prepared by etching micro-channels into the surface. Additionally, samples 1 and 2 included a PDMS surface coating to impart the hydrophobicity to the surface while sample 3 was without such coating. Data of the critical air-flow rate were then measured for different droplet sizes and plotted for the various surfaces as shown in Figs. 9 and 10. Unless otherwise noted, the micro-channels were aligned parallel to gravity. Thus, the air flow force was perpendicular to the channels. Fig. 9 shows that the hydrophilic surface (sample 3) required larger air-flow rates to cause droplet motion than the baseline surface for droplet volumes between 5 and 25 μL . (i.e. The drag force required to move the droplet along the surface in the direction of the air flow is higher on sample 3 than on the baseline surface.) In other words, droplets of comparable size are less likely to be “blown off” the back side of a heat exchanger constructed using the hydrophilic aluminum sample as compared to the baseline case. This results because surface roughness amplifies the underlying wettability of a surface. In this case, the surface was naturally hydrophilic and droplets wetted the surface so the micro-channels served to increase the surface hydrophilicity.

If the surface is processed with micro-channels and PDMS coating, it becomes hydrophobic (i.e. smaller contact angle hysteresis and smaller critical inclination angles). Fig. 10 shows that the surface with the micro-channels and PDMS coating reduces the critical air-flow force as compared to the baseline surface. Thus, a larger range of droplet sizes may be removed and droplets condensed on the surface may be removed while they are still

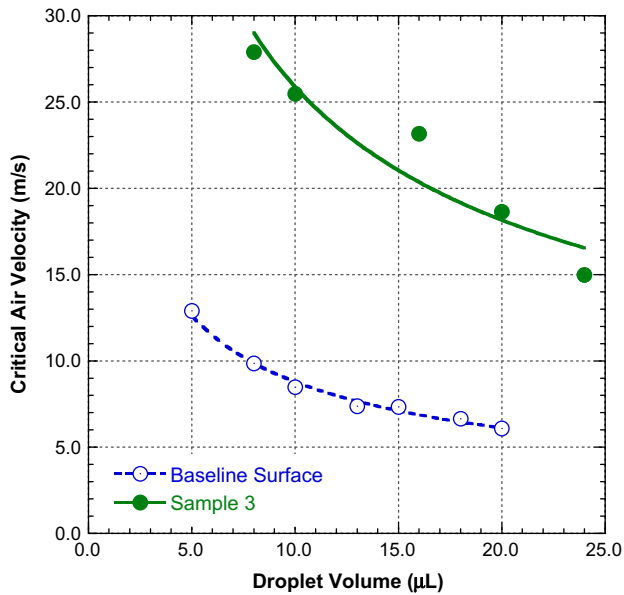


Fig. 9. Experimental data showing larger required critical air velocities on the anisotropic hydrophilic surface versus the baseline surface.

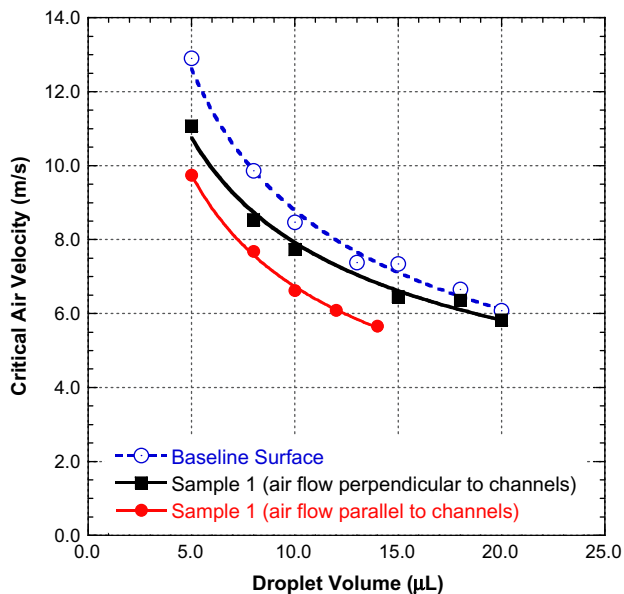


Fig. 10. The air flow rate necessary for droplet movement across the micro-channels was 1.0–1.2 m/s higher than the air flow rate for droplet movement along the channels.

relatively small. Thus, large droplets which tend to increase the core pressure drop are less likely to be retained on the surface. The surface micro-structure was also observed to suppress droplet movement across the grooves while at the same time facilitating movement along the grooves since the critical air-flow rates parallel to the channels were smaller than for droplet movement perpendicular to the channels. More specifically, the required air-flow rate for movement across the channels was 1.0–1.2 m/s larger than the air-flow rate for movement along the channels and only slightly lower than the baseline case. Depending on the application, either the hydrophilic surface (which would minimize condensate carryover) or the hydrophobic surface (which would help reduce the core pressure drop by facilitating condensate drainage downwards with gravity) may be more desired. In both cases,

the micro-channels provide a preferential direction and path for the water to drain.

Next, the new model was tested for its accuracy in predicting the onset of droplet departure. For the baseline surface (i.e. $\theta_A = 107.1^\circ$, $\theta_R = 75.2^\circ$, $\psi = 1$), the model was tested for the droplet volume range from 5 to 20 μL . The results are shown below in Fig. 11 with respect to the experimental data. Generally good agreement was observed. This agreement, however, was expected since the scaling factor, A , was determined in part using these data. These data are also in excellent agreement with Sommers and Jacobi [42] which found that for droplets 20 μL in size and larger, the droplet drains freely under the influence of gravity on vertical aluminum surfaces. (i.e. No air flow force is needed to initiate drainage.) The average error for these data was 12.3%.

Next, the model was applied to a few different anisotropic surfaces—namely, sample 1, sample 2, and sample 3. Sample 1 which was hydrophobic contained micro-channels (i.e. $w_1 = 40 \mu\text{m}$, $w_2 = 60 \mu\text{m}$ and $\delta = 10 \mu\text{m}$) and a PDMS coating. For these nominally 50 μm wide channels, the roughness parameter, ψ , was calculated and found to be 1.20. Fig. 12 shows the model predictions for sample 1 with respect to the experimental data. These results show that model agreement was similar to the baseline surface. The average error for this sample was found to be 7.0%. Thus, the dimensionless parameter ψ used to describe the topographical microstructure of the surface appears to capture some of the underlying physics. However, it should be noted that ψ is a two-dimensional representation of the contact line and as such may not accurately reproduce the three-phase contact line on highly tortuous surfaces.

Sample 2 also had micro-channels of nominally the same width (channel depth = 6.8 μm) and PDMS coating (see Table 2). For this surface, the value of ψ was 1.136. The model predictions for sample 2 together with the experimental data are shown in Fig. 13. For droplets less than or equal to 15 μL in size, the average error of these predictions was 23.5%. Although the agreement was not as good as sample 1, the overall trend was predicted well. Although sample 1 was more hydrophobic than sample 2 due to the increased channel depth, it should also be noted that sample 2 required smaller air-flow velocities for droplet removal. One explanation is that droplets can move more freely across the channels on sample 2 because the channels are shallower (i.e. less droplet pinning). Thus, the critical air velocity for droplet departure is reduced.

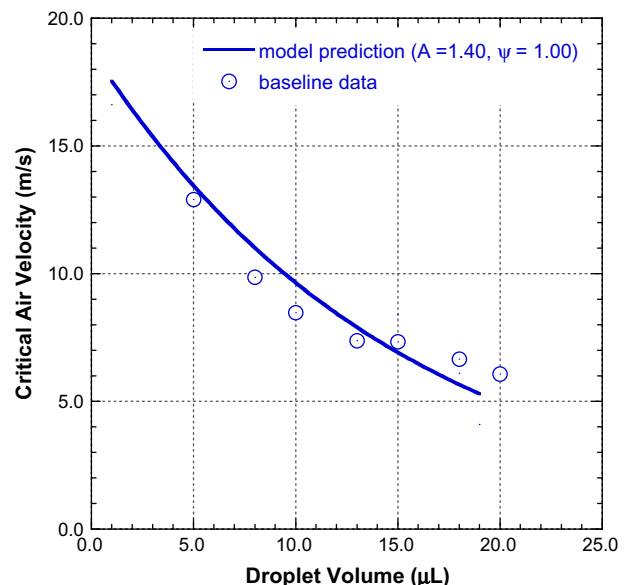


Fig. 11. Model prediction results for the baseline surface.

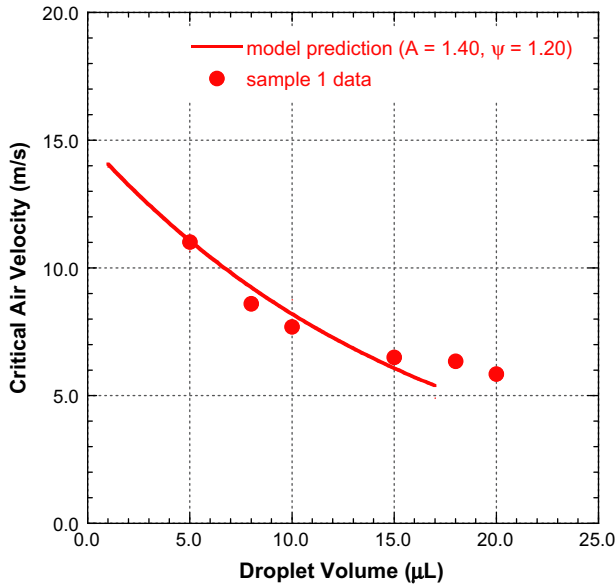


Fig. 12. Model prediction results for sample 1.

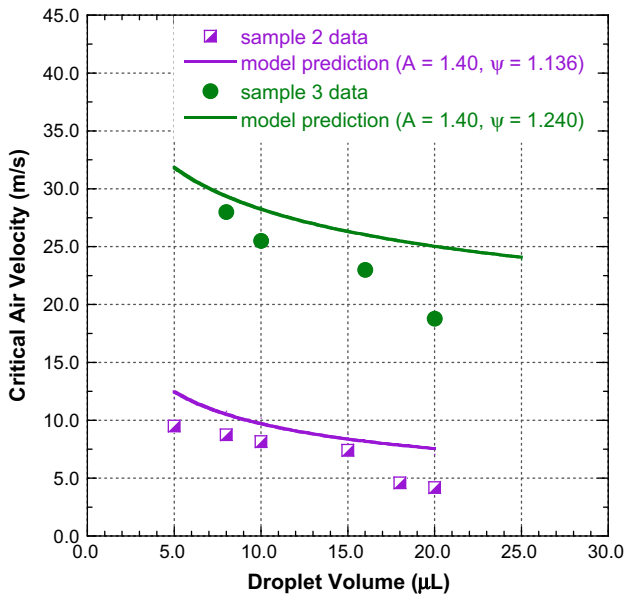


Fig. 13. Model prediction results for samples 2 and 3 showing the large difference in the critical air flow rate between these anisotropic hydrophilic and hydrophobic surfaces.

Sample 3 also had micro-channels ($w_1 = 36 \mu\text{m}$, $w_2 = 64 \mu\text{m}$, $\delta = 12 \mu\text{m}$) but no chemical coating. Thus, this surface was hydrophilic. For this surface, it was found that $\psi = 1.24$. Without any chemical coating, the wettability of sample 3 was only modified by the surface roughness. The predictions provided by the model agreed relatively well with the experimental data (see Fig. 13). The average error for these predictions was 25.0%. Because the surface was hydrophilic, significantly higher air velocities were needed to reach the critical state. In fact, the critical air velocities associated with droplet departure were more than 184% higher for sample 3 than the baseline surface.

By applying the model to multiple surfaces (both hydrophilic and hydrophobic) and comparing these results with experimental data, it can be concluded that the model is fairly robust and useful for predicting trends associated with the overall wettability of

aluminum fin surfaces. Using only a few simple inputs (i.e. contact angles and a roughness parameter), the model has been shown to predict changes in surface wettability on both homogeneous aluminum surfaces and enhanced surfaces containing parallel channels tens of microns in width and depth. The model also highlights the advantages of this particular anisotropic surface structure and thus can be used as a tool in the design of future micro-channel surface geometries.

Because it only requires four inputs (i.e. V , θ_{adv} , θ_{rec} , ψ), the model can also be easily used for exploratory purposes. If the advancing and receding contact angles are not known *a priori*, these angles may be predicted for a surface using a published equation of wetting. For example, two models are often used to describe how a droplet forms on a rough surface. A droplet that completely wets the surface and fills in the surface asperities is usually described by Wenzel's theory of wetting such that

$$\cos \theta' = r \cos \theta \quad (23)$$

where θ' is the apparent static contact angle of the droplet wetting the surface and r is the surface roughness factor defined as the ratio of the actual wetted area to the geometric projected area [43]. In this way, r is equivalent to ψ , and this ratio always has a value greater than or equal to unity. The second type known as the "composite surface" occurs when the droplet is suspended over the asperities, leaving air trapped beneath it. This form of wetting frequently occurs when the droplet is injected by syringe onto a surface having sufficiently small surface features. "Composite surfaces" are described by Cassie-Baxter's theory of wetting where

$$\cos \theta' = -1 + \varphi(\cos \theta + 1) \quad (24)$$

and φ represents the surface area fraction of the wetted area to the projected area [44]. This fraction always has a value less than unity.

In this study, the examined surfaces exhibited Wenzel's mode of wetting. Thus, as a first-order approximation, the advancing and receding contact angles of these micro-grooved samples can be predicted by simply knowing the advancing and receding contact angles (i.e. θ_{adv} , θ_{rec}) for a bare aluminum surface and an aluminum surface with a PDMS coating as shown in Table 6. More specifically,

$$\cos \theta_{\text{adv}}^* = \psi \cos \theta_{\text{adv}} \quad (25)$$

$$\cos \theta_{\text{rec}}^* = \psi \cos \theta_{\text{rec}} \quad (26)$$

where θ_{adv}^* is the predicted advancing contact angle and θ_{rec}^* is the predicted receding contact angle. If these predicted contact angles were used in the model along with the roughness parameter ψ , the critical air velocity is still predicted with a high level of accuracy as shown in Fig. 14. In this approach, only the surface roughness parameter ψ and the droplet volume V are specified as inputs to the model along with the homogeneous surface contact angles (which could be retrieved from other sources). It should be noted, however, that the Wenzel [43] and Cassie-Baxter equations [44] were originally developed for predicting static contact angles (not advancing and receding contact angles) on flat rough surfaces. Thus, although others have adopted this approach [45–47] and reasonable agreement has typically been observed, the physical basis for this approach (i.e. substituting $\theta = \theta_{\text{adv}}$) is not entirely clear. Other models have been suggested; however, most of these have been developed for super-hydrophobic surfaces and constitute modified forms of the Cassie-Baxter equation [48,49].

The model presented in this paper and the accompanying experimental results which show the promise of these functionalized surfaces for improved condensate management could be used in a wide range on engineering applications. Its utility, however, is of special relevance in air-cooling applications where condensate

Table 6
Contact angle predictions using Wenzel's model of wetting.

	ψ	Advancing angle (°)	% Error	Receding angle (°)	% Error
Aluminum + PDMS coating ^a	–	119.4	–	90.0	–
Sample 1 (predicted)	1.200	126.1	8.3%	90.0	0.4%
Sample 2 (predicted)	1.136	123.9	1.3%	90.0	2.3%
Aluminum surface ^b	–	86.8	–	45.8	–
Sample 3 (predicted)	1.240	86.0	15.9%	30.2	4.7%

^a Measured.
^b Liu et al. [50].

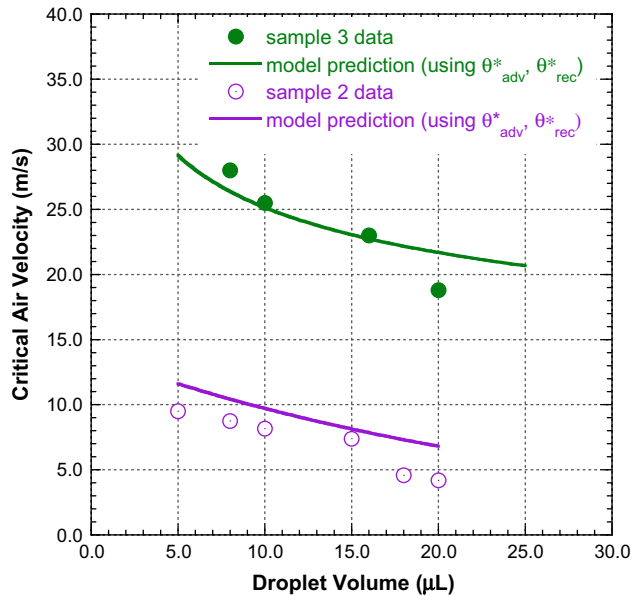


Fig. 14. Model prediction results for samples 2 and 3 determined using Wenzel's model of wetting to approximate the advancing and receding contact angles on these surfaces.

forms on the heat transfer surface. Because of its ability to accurately predict the critical air velocity for water droplet departure, this new calculation method could be used to facilitate the design of more robust, anisotropic water-shedding surfaces—surfaces that mitigate the potential for condensate “blow-off” in application.

8. Conclusions

A methodology for calculating the critical air velocity for water droplet departure from a vertical fin surface in cross flow was presented. This model which considers the combined effect of the gravitational, surface tension, and air flow forces on a droplet was found to provide reasonably accurate agreement with experimental data for water droplets 1–25 µL in size. In this method, the user must specify four inputs—namely, the advancing and receding contact angles of the surface, droplet volume, and a roughness parameter if applicable (i.e. θ_{adv} , θ_{rec} , V , ψ). When applied to surfaces of varying wettability, the model was shown to calculate the critical air velocity to within 15.2% for 89% of the droplets analyzed.

The model was then applied to surfaces containing parallel micro-channels aligned vertically with gravity with and without a hydrophobic coating. For surfaces with the hydrophobic coating, both improved condensate drainage behavior and increased resistance to condensate carryover were observed. That is these surfaces exhibited an ability to not only impede condensate droplet

departure in the streamwise direction but also an ability to facilitate improved condensate drainage in the direction of the channels. More specifically, for micro-grooved samples with a PDMS coating, the required air-flow rate for movement across the channels was 1.0–1.2 m/s larger than the air-flow rate required for movement along the channels and only slightly lower than the baseline case. For surfaces with no surface coating, the critical air velocity for water droplet departure was found to be more than 180% higher than the baseline surface—a behavior that was observed both numerically and experimentally. These results suggest that micro-grooved, anisotropic surfaces may be useful for resisting condensate carryover in air cooling applications where the surface micro-channels are aligned parallel to gravity to assist in condensate drainage.

Acknowledgements

The authors gratefully acknowledge support from the American Society of Heating, Refrigerating, and Air-Conditioning Engineers (ASHRAE New Investigator Award) and Sapa Heat Transfer.

References

- [1] J.F. Oliver, C. Huh, S.G. Mason, The apparent contact angle of liquids on finely-grooved solid surfaces – a SEM study, *J. Adhesion* 8 (1977) 223–234.
- [2] M. Morita, T. Koga, H. Otsuka, A. Takahara, Macroscopic-wetting anisotropy on the line-patterned surface of fluoroalkylsilane monolayers, *Langmuir* 21 (2005) 911–918.
- [3] Z. Yoshimitsu, A. Nakajima, T. Watanabe, K. Hashimoto, Effects of surface structure on the hydrophobicity and sliding behavior of water droplets, *Langmuir* 18 (2002) 5818–5822.
- [4] R.D. Narhe, D.A. Beysens, Nucleation and growth on a superhydrophobic grooved surface, *Phys. Rev. Letters* 93 (2004) 076103.
- [5] Y. Chen, B. He, J. Lee, N.A. Patankar, Anisotropy in the wetting of rough surfaces, *J. Colloid Interface Sci.* 281 (2005) 458–464.
- [6] C.W. Extrand, Y. Kumagai, Liquid drops on an inclined plane: the relation between contact angles, drop shape, and retentive force, *J. Colloid Interface Sci.* 170 (1995) 515–521.
- [7] R. Tadmor, K. Chaurasia, P.S. Yadav, A. Leh, P. Bahadur, L. Dang, W.R. Hoffer, Drop retention force as a function of resting time, *Langmuir* 24 (2008) 9370–9374.
- [8] R. Tadmor, P. Bahadur, A. Leh, H.E. N'guessan, R. Jaini, L. Dang, Measurement of lateral adhesion forces at the interface between a liquid drop and a substrate, *Phys. Rev. Letters* 103 (2009) 266101.
- [9] P. Dimitrakopoulos, J.J.L. Higdon, On the gravitational displacement of three-dimensional fluid droplets from inclined solid surfaces, *J. Fluid Mech.* 395 (1999) 181–209.
- [10] V.E.B. Dussan, R.T.-P. Chow, On the ability of drops or bubbles to stick to non-horizontal surfaces of solids, *J. Fluid Mech.* 137 (1983) 1–29.
- [11] V.E.B. Dussan, On the ability of drops or bubbles to stick to non-horizontal surfaces of solids. Part 2. Small drops or bubbles having contact angles of arbitrary size, *J. Fluid Mech.* 151 (1985) 1–20.
- [12] V.E.B. Dussan, On the ability of drops to stick to surfaces of solids. Part 3. The influence of the motion of the surrounding fluid on dislodging drops, *J. Fluid Mech.* 174 (1987) 381–397.
- [13] H. Merte Jr., S. Son, Further considerations of two-dimensional condensation drop profiles and departure sizes, *Wärme-und Stoffübertragung* 21 (1987) 163–168.
- [14] H. Merte Jr., C. Yamali, Profile and departure size of condensation drops on vertical surfaces, *Wärme-und Stoffübertragung* 17 (1983) 171–180.
- [15] A.I. El Sherbini, A.M. Jacobi, Liquid drops on vertical and inclined surfaces: I. An experimental study of drop geometry, *J. Colloid Interface Sci.* 273 (2004) 556–565.

- [16] A.I. El Sherbini, A.M. Jacobi, Liquid drops on vertical and inclined surfaces: II. A method for approximating drop shapes, *J. Colloid Interface Sci.* 273 (2004) 566–575.
- [17] C. Korte, A.M. Jacobi, Condensate retention effects on the performance of plain-fin-and-tube heat exchangers: Retention data and modeling, *J. Heat Transfer* 123 (2001) 926–936.
- [18] R.A.M. Al-Hayes, R.H.S. Winterton, Bubble diameter on detachment in flowing liquids, *Int. J. Heat Mass Transf.* 24 (2) (1981) 223–230.
- [19] W.G.J. Van Helden, C.W.M. Van Der Geld, P.G.M. Boot, Forces on bubbles growing and detaching in flow along a vertical wall, *Int. J. Heat Mass Transfer* 38 (11) (1995) 2075–2088.
- [20] G.B. Wallis, The terminal speed of single drops or bubbles in an infinite medium, *Int. J. Multiphase Flow* 1 (1974) 491–511.
- [21] R. Clift, J.R. Grace, M.E. Weber, *Bubbles, Drops, and Particles*, Academic Press, New York, 1978.
- [22] A.R. Khan, J.F. Richardson, The resistance to motion of a solid sphere in a fluid, *Chem. Eng. Commun.* 62 (1987) 135–150.
- [23] A. Tomiyama, I. Kataoka, I. Zun, T. Sakaguchi, Drag coefficients of single bubbles under normal and micro-gravity conditions, *JSME Int. J. Series B-Fluids Therm. Eng.* 41 (1998) 472–497.
- [24] R. Situ, T. Hibiki, M. Ishii, M. Mori, Bubble lift-off size in forced convective subcooled boiling flow, *Int. J. Heat Mass Transfer* 48 (2005) 5536–5548.
- [25] G. Duhar, C. Colin, Dynamics of bubble growth and detachment in a viscous shear flow, *Phys. Fluids* 18 (2006) 077101.
- [26] C. Antonini, F.J. Carmona, E. Pierce, M. Marengo, A. Amirfazli, General methodology for evaluating the adhesion force of drops and bubbles on solid surfaces, *Langmuir* 25 (11) (2009) 6143–6154.
- [27] M. Ishii, T.C. Chawla, Local drag laws in dispersed two-phase flow, Argonne, Report Anl-79-105, vol. 52, 1979.
- [28] L. Prandtl, *Hydroaeromechanics* [Russian translation], Foreign Literature Publishers, Moscow, 1949.
- [29] M.S. Volynskii, Study of droplet breakings in a gas flow, *DAN SSSR*, vol. 18(2), 1949.
- [30] W.R. Lane, Breakup of droplets in an air flow, *Ind. Eng. Chem.* 43 (6) (1951).
- [31] B.P. Volgin, F.S. Yugai, Experimental determination of the drag coefficient of a liquid droplet in the process of deformation and breakup in a turbulent gas flow, *Zhurnal Prikladnoi Mekhaniki i Tekhnicheskoi Fiziki* 9 (1) (1968) 152–156.
- [32] P.H.T. Uhlherr, C.G. Sinclair, The effect of free-stream turbulence on the drag coefficient of a sphere, In: *Chemeca '70: A Conference Convened by the Australian National Committee of the Institution of Chemical Engineers and the Australian Academy of Science*, Melbourne and Sydney, August 19–26, 1970.
- [33] W.D. Warnica, M. Renksizbulut, A.B. Strong, Drag coefficients of spherical liquid droplets Part 2: Turbulent gaseous fields, *Exp. Fluids* 18 (1995) 265–276.
- [34] S.A. Morsi, A.J. Alexander, An investigation of particle trajectories in two-phase flow system, *J. Fluid Mech.* 55 (1972) 193–208.
- [35] K.V. Beard, H.R. Pruppacher, Determination of the terminal velocity and drag of small water drops by means of a wind tunnel, *J. Atmos. Sci.* 26 (1969) 1066.
- [36] R. Mei, J.F. Klausner, Unsteady force on a spherical bubble at finite Reynolds number with small fluctuations in the free-stream velocity, *Phys. Fluids A* 4 (1992) 63–70.
- [37] J.F. Klausner, R. Mei, D.M. Bernhard, L.Z. Zeng, Vapor bubble departure in forced convection boiling, *Int. J. Heat Mass Transfer* 36 (1993) 651–662.
- [38] L.Z. Zeng, J.F. Klausner, D.M. Bernhard, R. Mei, A unified model for the prediction of bubble detachment diameters in boiling systems: Part II flow boiling, *Int. J. Heat Mass Transfer* 36 (9) (1993) 2271–2279.
- [39] Z.G. Guo, F. Zhou, J. Hao, W. Liu, Effects of system parameters on making aluminum alloy lotus, *J. Colloid Interface Sci.* 303 (2006) 298–305.
- [40] Preeti.S. Yadav, Prashant. Bahadur, Rafael. Tadmor, Kumud. Chaurasia, Aisha. Leh, Drop retention force as a function of drop size, *Langmuir* 24 (2008) 317–318.
- [41] A.D. Sommers, A.M. Jacobi, Wetting phenomena on micro-grooved aluminum surfaces and modeling of the critical droplet size, *J. Colloid Interface Sci.* 328 (2) (2008) 402–411.
- [42] A.D. Sommers, A.M. Jacobi, Creating micro-scale surface topology to achieve anisotropic wettability on an aluminum surface, *J. Micromech. Microeng.* 16 (8) (2006) 1571–1578.
- [43] T.N. Wenzel, Resistance of solid surfaces to wetting by water, *Ind. Chem. Eng.* 28 (8) (1936) 988–994.
- [44] A.B.D. Cassie, S. Baxter, *Trans. Faraday Soc.* 40 (1944) 546–551.
- [45] J. Bico, C. Marzolin, D. Quere, Pearl drops, *Europhys. Lett.* 47 (2) (1999) 220–226.
- [46] N. Patankar, On the modeling of hydrophobic contact angles on rough surfaces, *Langmuir* 19 (2003) 1249–1253.
- [47] Y. Kwon, S. Choi, N. Anantharaju, J. Lee, M.V. Panchagnula, N.A. Patankar, Is the Cassie–Baxter formula relevant?, *Langmuir* 26 (22) (2010) 17528–17531.
- [48] W. Choi, A. Tuteja, J.M. Mabry, R.E. Cohen, G.H. McKinley, A modified Cassie–Baxter relationship to explain contact angle hysteresis and anisotropy on non-wetting textured surfaces, *J. Colloid Interface Sci.* 339 (2009) 208–216.
- [49] A. Horsthemke, J. Schröder, *J. Chem. Ing. Tech.* 53 (1981) 62.
- [50] L. Liu, A.M. Jacobi, D. Chvedov, A surface embossing technique to create micro-grooves on an aluminum fin stock for drainage enhancement, *J. Micromech. Microeng.* 19 (2009) 035026.